PNAS
www.pnas.org

Supplementary Information for

Geometry and dynamics link form, function and evolution of finch beaks

Salem Al-Mosleh, Gary P. T. Choi, Arkhat Abzhanov and L. Mahadevan

L. Mahadevan.
E-mail: lmahadev@g.harvard.edu.

This PDF file includes:

Other supplementary materials for this manuscript include the following:

Movie S1. Comparison of three-dimensional models. The four meshes shown are (1) the entire skull, (2) the cut out upper surface of the beak, (3) the generated sections from the cellular model and (4) the generated cross sections from the mean curvature flow.

Movie S2. Growth generated using the boundary & bulk death model as described in Fig. S12.

Movie S3. Modified mean curvature flow with circular cross sections. Growth generated as described in the text for parameters taken from a C. *pallidus* sample.

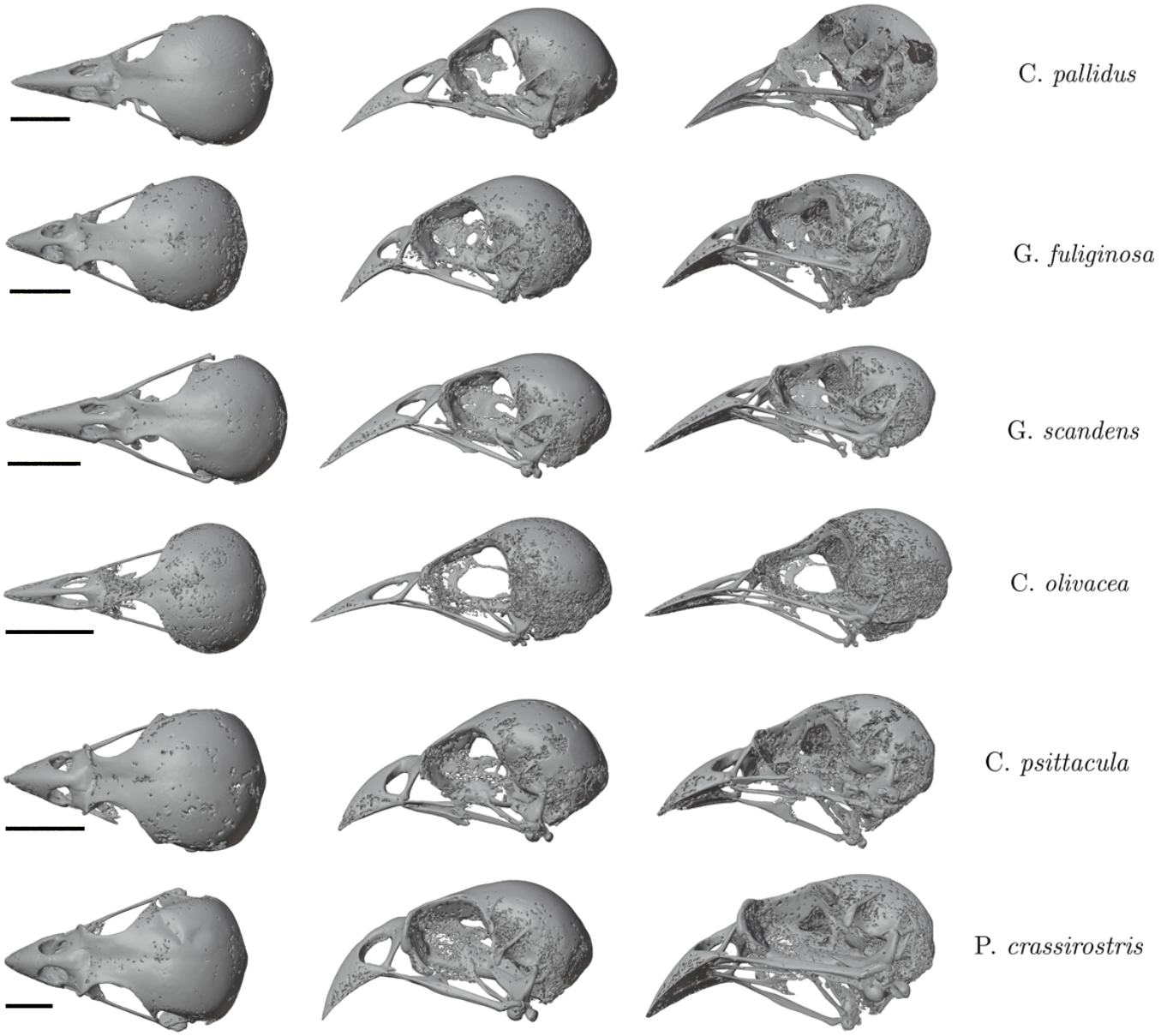

Fig. S1. Different views of the skulls from different species used in our study. The skulls are shown from the top, side and lateral-bottom views. Scale bars, 10mm.

Supporting Information Text

Mesh Preprocessing. Fig. S1 shows several raw skull models from different species used in our study. The cutting procedures applied to the 3D models of the skulls were shown in Fig. 1B of the main text. (1) The skulls are first aligned according to their principal moment directions* in such a way that the direction of highest moment is along the x-axis and the lowest is along the z-axis. (2) The beak is then cut with a plane perpendicular to the x-direction and then aligned again according to the beak's own moment directions. The cut captures as large a part of the beak as possible without including bones not belonging to the beak. (3) We employ a voxelization and smoothing method (1) to generate an approximation of the beak that is smoother and watertight, without holes (more information below). The results of this smoothing process may also be scaled in the x, y and z directions manually to achieve even closer agreement with the original mesh. (4) In order to get a single valued height function to represent the beak, we take the watertight mesh and cut out the top part of it using the lowest horizontal plane not containing the lower surface of the upper beak (palate). The majority of the analysis in the main text was performed on this "top mesh". We place the origin of the coordinate system at the tip of the cut beak and assume the axes are oriented along the principal moment directions.

Now we describe the voxelization and smoothing method we used for producing smooth and watertight meshes without

*The principal moment directions for a point cloud are defined as eigen-directions of the moment tensor $M_{ij} = \sum_{n=1}^{N} \left(\mathbf{P}_n \cdot \mathbf{P}_n \, \delta_{ij} - \mathbf{P}_{ni} \, \mathbf{P}_{nj} \right)$, where $\mathbf{P}_n$ is the position of point n, N is the total number of points and the indices i, j refer to the (x, y, z)-axes and δ_{ij} are the components of the identity matrix.

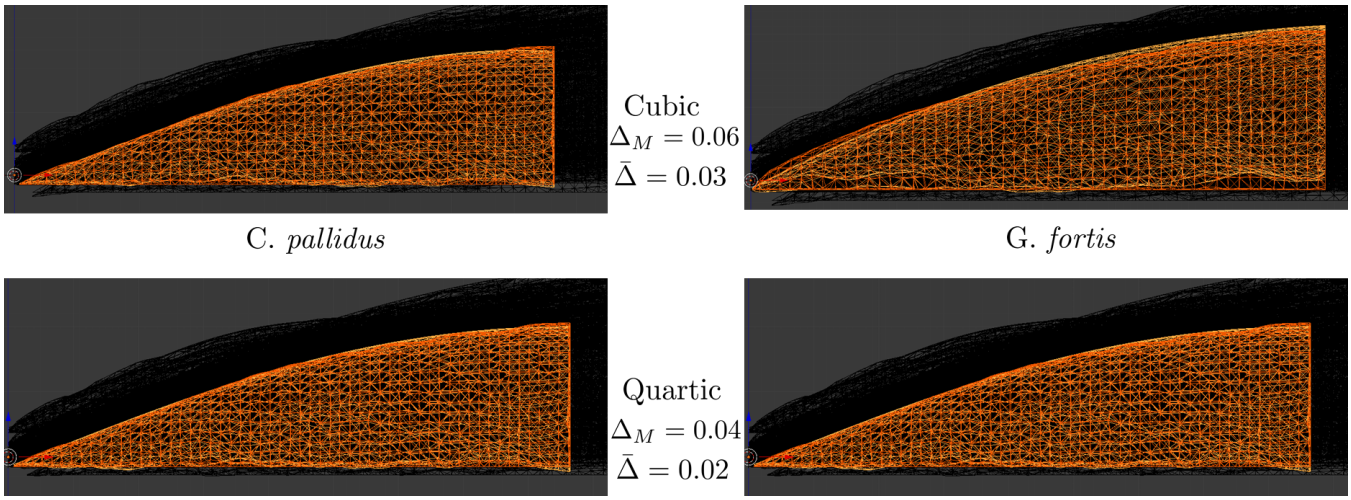

Fig. S2. Comparison between cubic and quartic fits. The top two figures compare the cubic fit (orange) to the original beak shape (yellow) for two different species. The lower two figures show the comparison for the quartic fit. These fits were obtained in Python using the SciPy package (7). The quartic fit is only slightly better than the cubic fit and we may work with either one. Beyond visual inspection, we can quantify how well all the fits capture the original meshes using the Modified Hausdorff Distance (MHD), a measure of how different two clouds of points are (8). The quantity Δ_M is the maximum MHD between any beak and its fit, normalized by a reference distance between two chosen samples. The reference distance is chosen to be the MHD between a G. *Fortis* and a G. *Magnirostris* sample. $\bar{\Delta}$ is the mean value over all such distances.

holes from the raw meshes. Given any raw triangulated mesh, we first convert it to a voxel volume using the `Polygon2Voxel` function available in the MATLAB Central File Exchange (2). We then compute an alpha shape of the voxel vertices using the MATLAB's built-in function `alphaShape` and extract the triangulation facets on the boundary of it using the MATLAB's built-in function `boundaryFacets`. Holes are subsequently filled using a medial axis approach (3). To enhance the smoothness of the resulting mesh, we apply an implicit Laplacian smoothing (4) with the cotangent Laplacian (5) used. Finally, we check and repair the resulting mesh using the `meshcheckrepair` function in the Iso2mesh toolbox (6), yielding a smooth and watertight (genus-0) mesh for our study.

In order to extract the transverse and midsagittal cross sections, we used a fit of the form $z = F(x, y)$ to interpolate the top mesh. Fig. S2 shows the performance of the fit when F is a cubic or quartic polynomial. In the cubic case, for example, we have

$$F(x,y) = c_1 + c_2\,x + c_3\,y + c_4\,x^2 + c_5\,x\,y + c_6\,y^2 + c_7\,x^3 + c_8\,x^2\,y + c_9\,x\,y^2 + c_{10}\,y^3, \qquad [S.1]$$

where all the c_i parameters are fitted constants.

Having a smooth interpolation of the beaks allows us to study cross sections in different directions. In particular, we look at the midsagittal ($y = 0$) and transverse ($x = constant$) cross sections. In both cases, we find the sections to be very well described by parabolic forms (see Figs. S3 & S4). Furthermore, we find that the Cartesian curvature of the transverse sections increases linearly with the distance in the x direction from the tip. These results are summarized by Eq. (1) in the main text.

Patterns in Morphospace. We start by looking at patterns among the various beak dimensions. As mentioned in the main text, when aligned according to the moment directions of the beak, the aspect ratios of all the beaks are very similar (see Fig. S5). This fact can be captured by the following correlations coefficients between the various beak dimensions,

$$Cor[L,W] = 0.92, \qquad Cor[D,W] = 0.95, \qquad Cor[L,D] = 0.92. \qquad [S.2]$$

If we instead consider the beak dimensions when aligned according to the principal directions of the entire skull, the aspect ratios vary considerably more across the different species (Fig. S5). The correlations now become

$$Cor[L,W] = 0.62, \qquad Cor[D,W] = 0.94, \qquad Cor[L,D] = 0.70. \qquad [S.3]$$

Therefore, a developmental mechanism could generate deeper and wider beaks by simply rotating the beak growth direction relative the head. Interestingly, the depth and width are still highly correlated as was discussed in Fig. 5B in the main text.

Fig. S5C shows the mean value for each species in the curvature morphospace defined by $(\tilde{\kappa}_x, \tilde{S})$. Note that G. *magnirostris* has normalized sharpening rate much bigger than the rest while C. *psittacula* has the largest normalized midsagittal curvature. In the case of G. *magnirostris*, we argue from mechanical consideration that a high sharpening rate gives the beak more rigidity and might explain this observation. As for C. *psittacula*, we also found from mechanical consideration that a higher midsagittal curvature gives a bigger force at the tip for same applied torque at the join (holding the dimensions fixed). Finally note that C. *olivacea* and C. *fusca* (insect eaters) occupy the lower end in terms of sharpening rate ($\tilde{S} \approx 4$) and the midsagittal curvature ($\tilde{\kappa}_x \approx 0.5$).

It was shown in (9) that by independent scaling transformations in the x and z directions, the shapes of beaks in species of the genus *Geospiza*, as well as *Camarhynchus*, can be collapsed into each other for each genera separately, whereas shearing

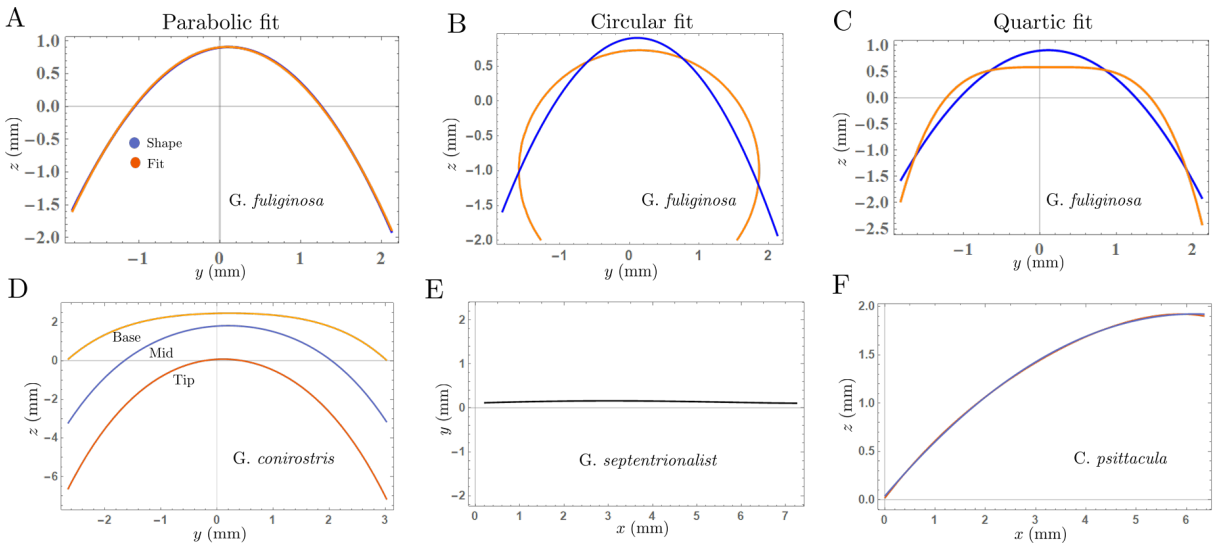

Fig. S3. Fitting beaks with Parabolas. Panels (A - C) show a transverse section halfway between the base and tip of a G. *fuliginosa* sample along with different fitting forms. (A) Shows the fit using the parabolic form $z = a_f(y-b_f)^2+c_f$, where (a_f, b_f, c_f) are fitting parameters. (B) shows the fit using the circular form $(z-a_f)^2+(y-b_f)^2 = c_f^2$. (C) shows the fit using the quartic form $z = a_f(y-b_f)^4 + c_f$. Note that only the parabolic fit works well across all transverse sections along the length of the beak for all samples. (D) The shape of three different transverse cross sections along the length of the beak, near the tip, the cutting plane (proximal end) and a plane directly between them. As we approach the tip, the curvature increases monotonically (see Fig. S4). The range of this plot in the $y-$direction is taken from the width of the beak at the base. (E) The point of maximum height (solution to $\partial z(x,y)/\partial y = 0$) on the parabolas in the xy-plane, which confirms that $y = 0$ gives approximately the center of the parabolas. (F) showing how closely the midsagittal section is fit by a parabola for a C. *psittacula* sample. The fit works similarly for all other samples. The figures labeled as "Shape" are obtained from the cubic or quartic fits described earlier (see Fig. S2). On the other hand, the blue curve represents a parabolic fit function.

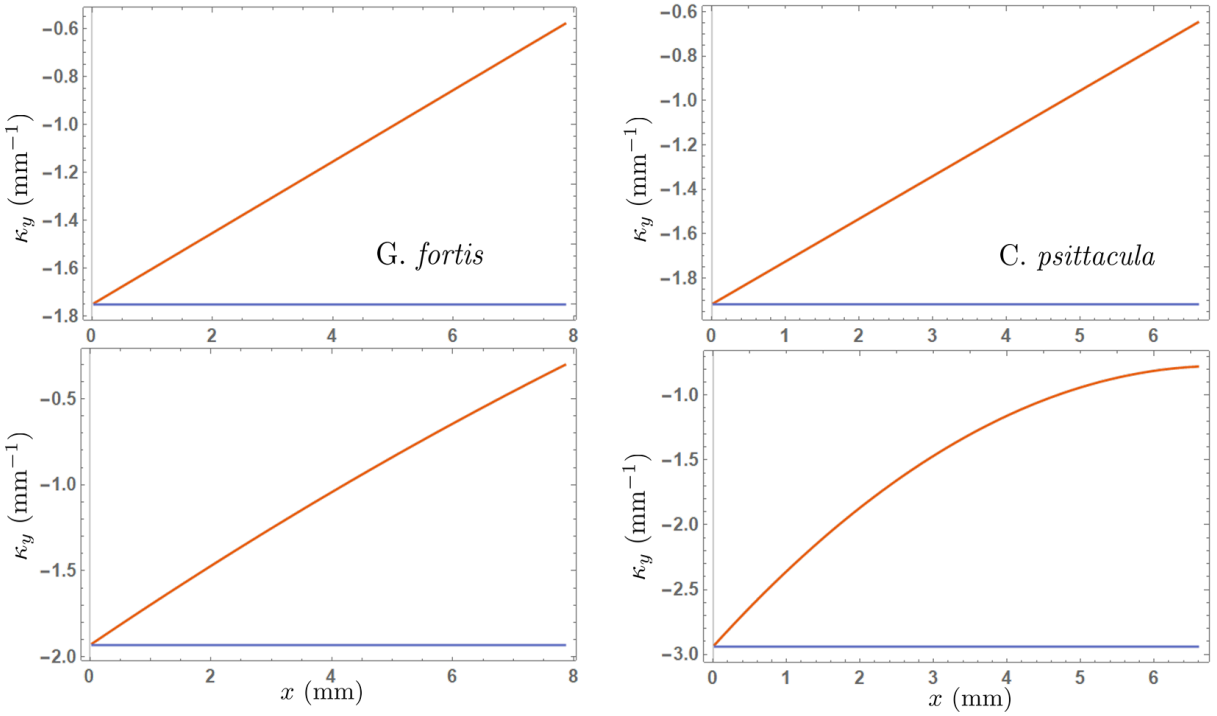

Fig. S4. The monotonic increase of curvature as we approach the tip. For the cubic approximation of the beak shape, transverse curvature always increases linearly (top row). In order to check whether this is a feature of the approximation or a true feature of the shape, we evaluate the same plots using the quartic fit. As can be seen from the two bottom rows, the increase is still approximately linear. The most extreme deviation from linearity of $\kappa_y(x)$ is for a C. *Psittacula* sample, the behavior of which is shown in the lower right plot. Even in this case, a linear approximation for $\kappa_y(x)$ would capture the shape reasonably well.

transformations are required to match the species from the different genera together. In the present case, since the midsagittal sections can be fit with parabolas, we can always collapse them to a common functional form by scaling transformations. For instance, if the shape of the midsagittal section is fit to $z = c\,x - \kappa_x\,x^2$ by rescaling $x \to l_x\,x$ and $z \to l_z\,z$, where $l_x = c/\kappa_x$ and $l_z = c^2/\kappa_x$ we get $z = x - x^2$. Therefore, we see that shear transformations are not required for midsagittal sections. In

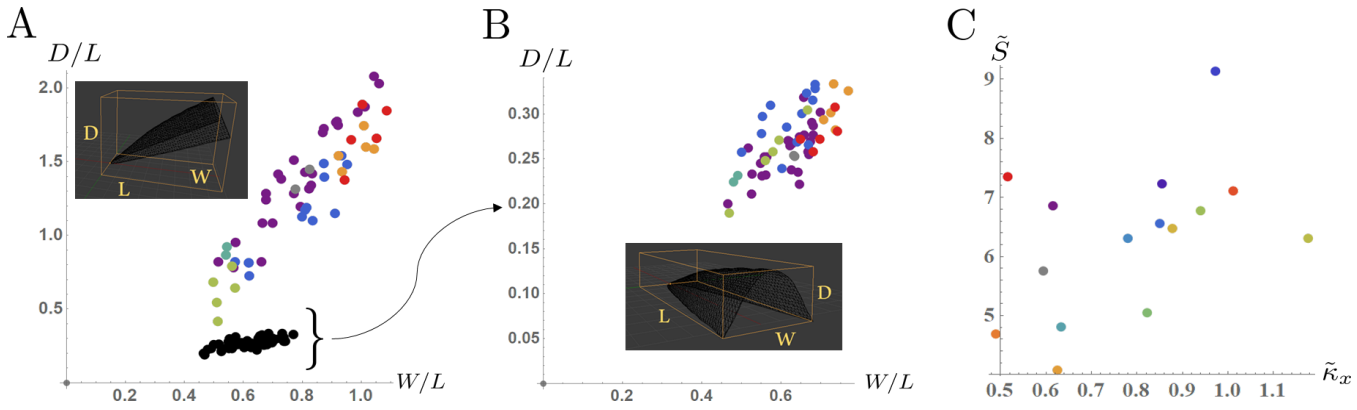

Fig. S5. Patterns in morphospace. (A) The colored points give the aspect ratios of all the samples, color coded according to genus as in the main text, when the beak is aligned according to the directions of the entire skull (inset). The black points give the results when the beak is aligned according to its own moment directions. Panel (B) shows those points in more detail, color coded as in (A). Panel (C) shows the pattern among the different species in curvature space color coded as in Fig. 1C in the main text. Each point is an average over the samples of the corresponding species. Note that G. *magnirostris* has the highest sharpening rate $\tilde{S}$ and C. *psittacula* has the highest midsagittal curvature. The two *Certhidea* species, in addition to the vampire finch, are on the lower end of both curvatures. This is the same information as in Fig. 2D in the main text.

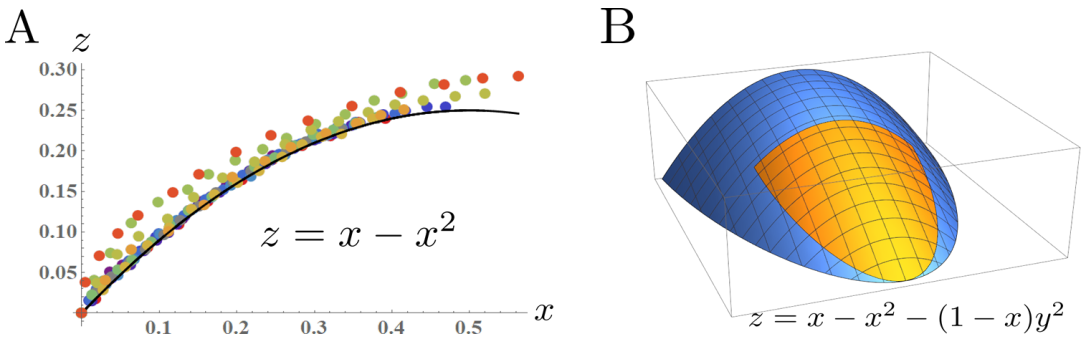

Fig. S6. Shear transformations collapse beak shape. (A) Using the midsagittal beak sections from (9) and fitting them with parabolic form, we are able to find scaling transformations that collapse all profiles onto a common functional form. (B) The use of affine transformations to collapse a beak shape described by Eq. (1) in the main text to the common form $z = x - x^2 - (1 - x)y^2$.

fact, if we not only match the functional forms, but the endpoints as well, then general affine transformation are necessary and sufficient to accomplish this (Fig. S6).

Now we ask whether affine transformations are sufficient to collapse beak shapes in 3D to a common form. Since the functional form of the beak (Eq. (1) in the main text) is cubic, it is not obvious what the answer should be. It turns out, with an affine transformation, it is possible to collapse all beaks onto the common functional form $z = 2x - x^2 - (1 - x)y^2$. However, it is not possible to ensure that the dimensions of the transformed shape are the same. For example, if we scale two beaks along the x-direction to make them have the same functional form, the lengths will not necessarily match between them (Fig. S6).

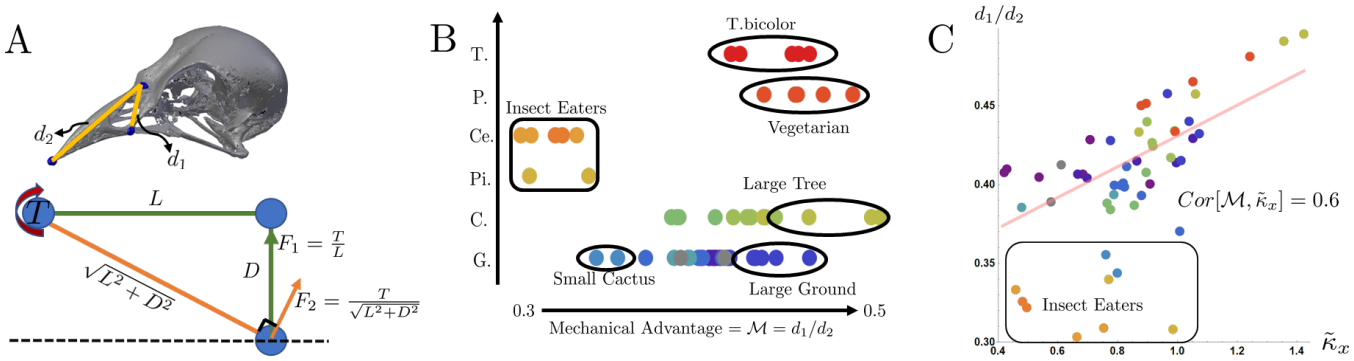

Fig. S7. Sagittal curvature enhances bite force. (A) An illustration of how for the same input torque T we get stronger output force by curving the beak (green vs orange lines). This could explain the curved nature of the tip-biting large tree finch. (B) The mechanical advantage calculated for all samples studied. Note how, as expected, insect eaters and the small cactus finch have low mechanical advantage whereas seed eaters and tip-biters score high on this measure. (C) The mechanical advantage plotted against the sagittal curvature which strengthens the case for the role of curvature in increasing the bite force as in panel (A).

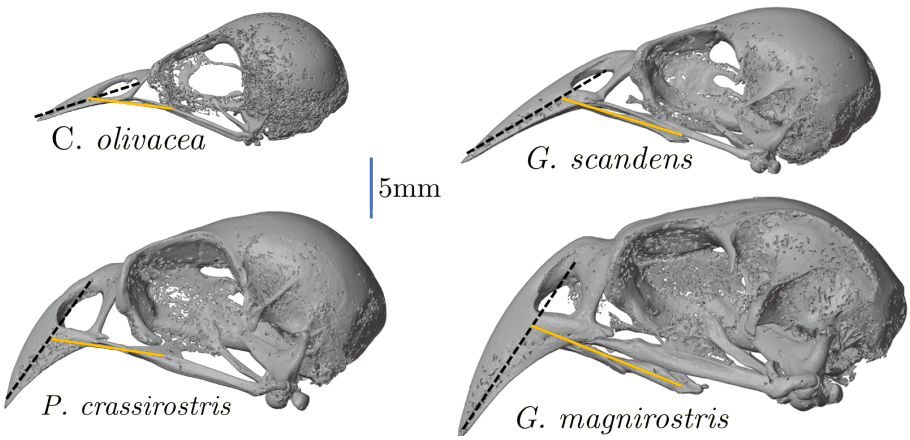

Fig. S8. Comparison of attachment angles of beaks. G. *magnirostris* and P. *crassirostris* have high angles between the skull and the beak, leading to approximately normal angles between the direction of attachment of palatine bones (similar results hold if we use the jugal bone since they attach in similar ways) to the beak and the major axis of the premaxilla. This leads to a higher output bite force for the same applied force from the muscles. Probing beaks on the other hand have more acute angles and straighter beaks.

Form and Function. The mechanical advantage is given by

$$\mathcal{M} \equiv \frac{|\mathbf{F}_{out}|}{|\mathbf{F}_{in}|} = \frac{d_1 \sin(\theta)}{d_2 \sin(\phi)},$$

where d_1 is the distance from the point of muscle force application to the joint, d_2 is the distance from joint to seed position, θ and ϕ are the corresponding angles shown in Fig. 3A in the main text.

Using the mechanical advantage ($\mathcal{M}$) enables us to explore the interplay between form and function. One feature that we found to be well correlated with $\mathcal{M}$ is the dimensionless midsagittal curvature $\tilde{\kappa}_x$ with the correlation coefficient being $Cor[\mathcal{M}, \tilde{\kappa}_x] = 0.6$. In Fig. S7 we can see a trend line between these two quantities with some notable outliers. The exceptions include C. *fusca*, C. *olivacea*, T. *bicolor* and the small cactus finch. For C. *fusca* and C. *olivacea* the mechanical advantage is smaller than would be predicted from the trend line, as expected for insect eaters, since lower mechanical advantage leads to faster closing speeds. Finally, for the case of the cactus finch, it may be expected that a longer narrower beak is efficient for probing, thus possibly explaining the fall off from the bite-force trend. The role that angle plays is highlighted in Fig. S8, and the dependence of mechanical advantage on beak shape and seed placement is highlighted in Fig. S9.

Generally speaking, the curvature of a mechanical structure, especially if it is thin, will play a role in determining its rigidity. For example, the sharpening rate is highest among G. *magnirostris*, which is known for cracking large tough seeds. In order to investigate the relation between curvature and rigidity we performed a simple numerical simulations of beak mechanics (Fig. S10). First the mesh is created using Mathematica's `ImplicitRegion` and `DiscretizeRegion` methods. In order to test the effect of the sharpening rate on its own we fix $W = L = D = 2$ $\kappa_x = 1$ and vary the sharpening rate in unit steps starting from zero. The edges of the mesh are treated as elastic springs from which a dynamical matrix and elastic energy is calculated. Then a force is applied at the tip of the beak as a linear term in the energy and the energy is minimized, keeping the base of the beak at a fixed position. Rigidity is defined as the inverse of the (mean) strain value and is normalized so that it is equal to one for the $S = 0$ beak. We see from the figure that as the sharpening rate increases, the rigidity (strain) goes up (down).

We may understand the role played by curvature in controlling the rigidity of a structure by considering the problem of

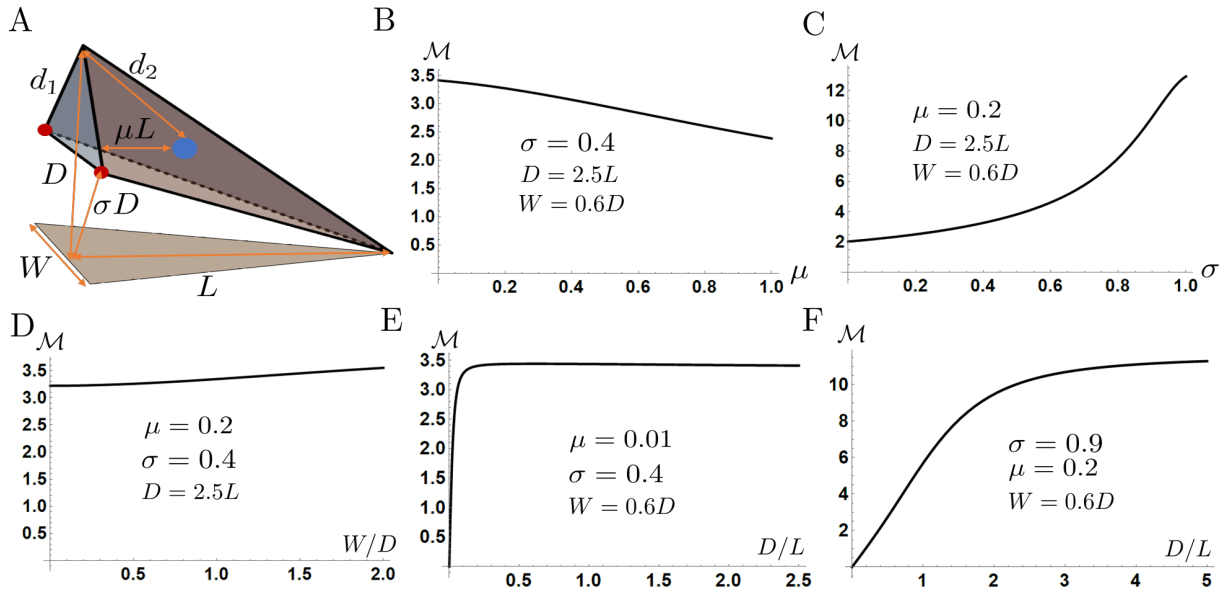

Fig. S9. Dependence of mechanical advantage on beak shape and seed placement. (A) The simple mechanical model of the beak shown in the main text. (B) The dependence of the mechanical advantage on seed placement. Note that smaller values lead to larger forces, which explains why seeds are placed in the back of the beak (10). Note that the slope would be smaller for larger values of D/L. (C) Increasing the parameter σ brings the point of force application close to the joint and therefore increases $\mathcal{M}$. However, for large values of σ the resulting beak will be more easily broken due to smaller attachment surface area. Furthermore, such values are difficult to achieve by simply rotating the beak relative to the skull. (D) The weak dependence of $\mathcal{M}$ on W/D. (E) The parameter μ also controls how fast the mechanical advantage saturates as a function of D/L so that lower values of μ lead to faster saturation. (F) On the other hand, higher values of the parameter σ lead to higher saturation magnitudes.

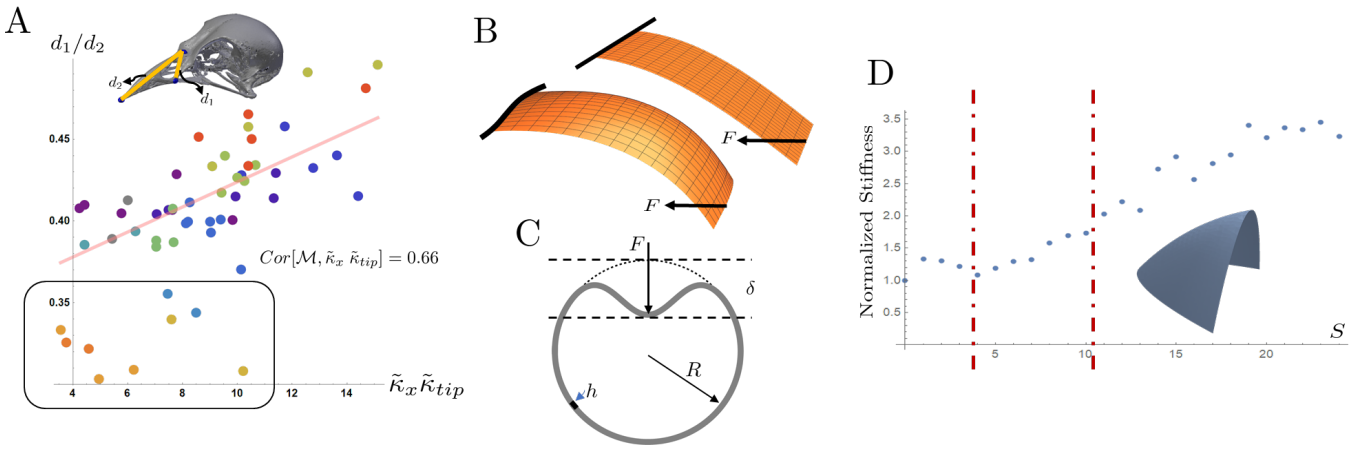

Fig. S10. Curvature enhances the rigidity of thin structures. (A) The relation between the mechanical advantage and the product of curvatures in the sagittal and transverse directions. The probing beaks are enclosed in the rectangle to highlight their different behavior (due to selection for longer straighter beaks). (B) A cartoon illustrating the role of curvature in enhancing rigidity. Under the applied force F, the upper shell will deform much more than the bottom one due to its transverse curvature. (C) We may also see the role played by curvature in enhancing rigidity by considering the problem of indenting a spherical shell. The effective rigidity in this case is proportional to the local curvature of the shell (11). (D) Simulation of rigidity of an elastic shell as function of sharpening rate as explained in the SI text. The increase in rigidity with S explains why a beak relying on strong bite force, like G. *magnirostris*, has the highest sharpening rate (Fig. S5).

indenting a sphere with a much smaller and very rigid (second) sphere. If the first sphere (sphere A with radius R_A, playing the role of the beak) is solidly filled and the second sphere (sphere B with radius R_B, playing the role of the seed) is pushed with a force F against it, then the answer to this problem has been given by Hertz in 1882 (12). Namely, the force over the displacement δ can be written as

$$K_H \equiv \frac{F}{\delta} \sim \frac{4}{3} E_A \sqrt{1 - \frac{R_B}{R_A}} \sqrt{R_B\, \delta}, \qquad [S.4]$$

where E_A is the Young modulus for sphere A. In writing this expression, we assumed $R_B \gg R_A$ for concreteness. In general, the expression in the square root should be replaced by $R\delta$, where $R = (R_A^{-1} + R_B^{-1})^{-1}$. Notice how the effective rigidity K_H increases as square root of the displacement (vanishing for $\delta = 0$) and increases with R_A. This suggests that for small displacements a large solid sphere may not present enough rigidity against indentation.

This behavior will change if the sphere A is an elastic shell with thickness h. In particular, as shown by Pogorelov (11), for

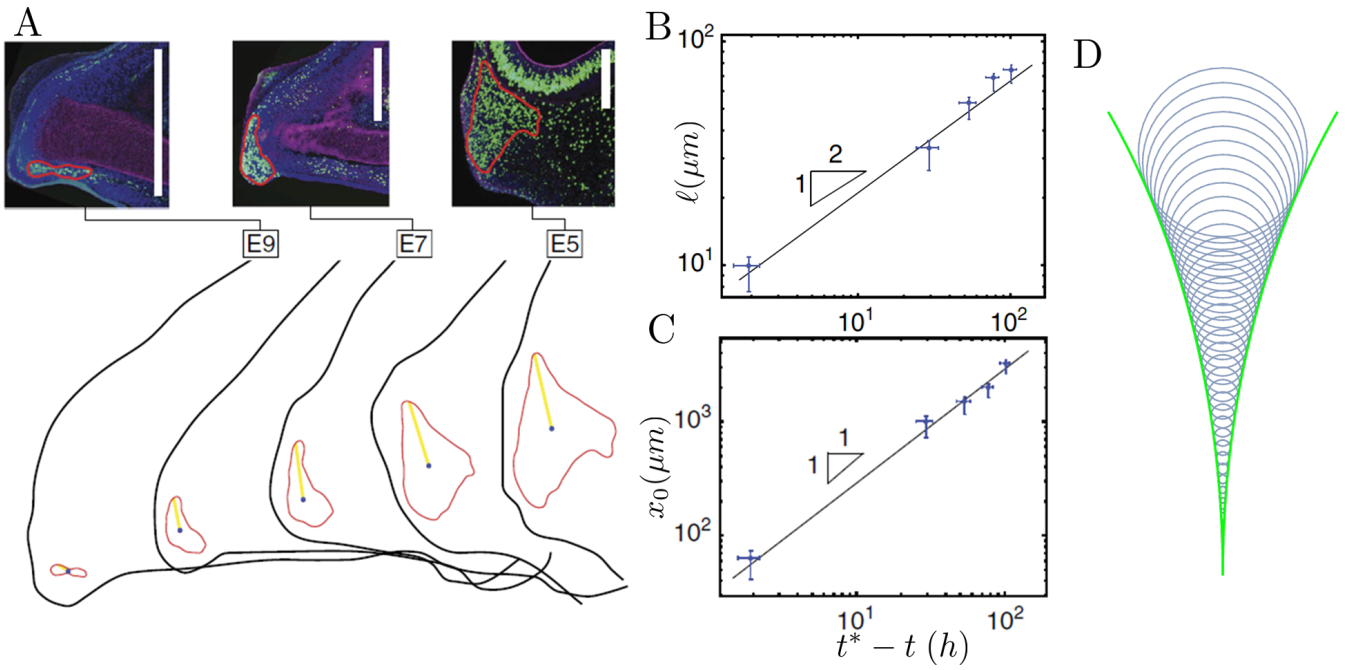

Fig. S11. Growth envelopes. (A) Experimental results from Ref. (9) showing the evolution of the growth zone. Scale bar, 0.5mm. The yellow line indicates the decaying size of the growth region which is plotted as a function of time in panel (B), while the blue dot indicates the position of the center of the growth zone which corresponds to panel (C). From the data in (B) we obtain $b \approx 22\mu\text{m}^2/h$, while from (C) we get $U \approx 29\mu\text{m}/h$. (D) A comparison of envelopes generated from Eq. (S.10), shown in green and the explicitly generated envelope from a sequence of growth regions shown in blue. Here we used the values $\alpha = 2, \beta = 0, \gamma = 1, p = 2$ and $q = 1$.

small displacements, $\delta < h$, the effective rigidity can be written as

$$K_P \sim \frac{E_A\, h^2}{R_A}. \qquad \text{[S.5]}$$

In this case we see that a shell becomes more rigid with increasing curvature $\kappa \equiv R_A^{-1}$. By equating the right hand sides of Eqs. (S.4-S.5), we may obtain the length scale at which these two rigidities become comparable:

$$K_H \sim K_P \implies R_A \sim \sqrt{\frac{h^2}{\delta\, R_B}}\, h \implies \delta \sim \frac{h^3}{R_B R_A^2} h. \qquad \text{[S.6]}$$

For small displacements and a small enough indenter, the rigidity of a spherical shell becomes larger than a solid sphere. This counter intuitive result seems to suggest that by taking away material from the inside of a sphere, it can become more rigid! The reason why this can happen is that stress distributions in response to indenting will be different in the two cases. For a solid sphere, the strain will be in a region of order $\sqrt{R_A \delta}$ (13), whereas in the case of a spherical shell, due to the balance of bending and stretching energies, it will spread out into a larger (for small δ) region of size $\sqrt{R_A h}$. This highlights the potential mechanical significance of a layered structured for beaks (14, 15).

Envelope of the Growth Zone. In (16), a 2D model of beak growth was proposed in which the beak shape is determined by how the size and position of the growth zone evolves over time. Mathematically, the growing region at any instant is the interior of the curve (surface in 3D) given by

$$G(\eta, \xi) = 0, \quad \text{where} \quad \eta(t) = \frac{x - x_0(t)}{\ell(t)} \quad , \quad \xi(t) = \frac{y - y_0(t)}{\ell(t)}, \qquad \text{[S.7]}$$

$$x_0(t) = \alpha(t_* - t)^q, \quad y_0(t) = \beta(t_* - t)^q \quad \text{and} \quad \ell(t) = \gamma(t_* - t)^p. \qquad \text{[S.8]}$$

Here the power law behavior (with constant parameters α, β, γ, p and q) is assumed for the center of the growth zone $(x_0(t), y_0(t))$ and its size $\ell(t)$. The shape of the beak is given by the envelope of all such growth regions (Fig. S11) over time and therefore will satisfy the equation $\partial_t G = 0$ in addition to $G = 0$. In order to express this equation in terms of x and y, we first calculate

$$\partial_t \eta \equiv \dot{\eta} = -\frac{\dot{x}_0}{\ell} - \frac{\dot{\ell}\,(x - x_0)}{\ell^2} = \frac{q\alpha(t_* - t)^{q-1}}{\gamma(t_* - t)^p} + \frac{p}{t_* - t}\eta = \left(\eta + \Lambda_\eta\,(t_* - t)^{q-p}\right)\frac{p}{t_* - t}, \qquad \text{[S.9]}$$

and similarly for $\dot{\xi}$. Here $\Lambda_\eta = \frac{\alpha\, q}{\gamma\, p}$ and $\Lambda_\xi = \frac{\beta\, q}{\gamma\, p}$. Therefore, the equation for the envelope becomes

$$\partial_t G = \dot{\eta}\, G_\eta + \dot{\xi}\, G_\xi = 0 \implies \left(\eta + \Lambda_\eta\,(t_* - t)^{q-p}\right) G_\eta + \left(\xi + \Lambda_\xi\,(t_* - t)^{q-p}\right) G_\xi = 0. \qquad \text{[S.10]}$$

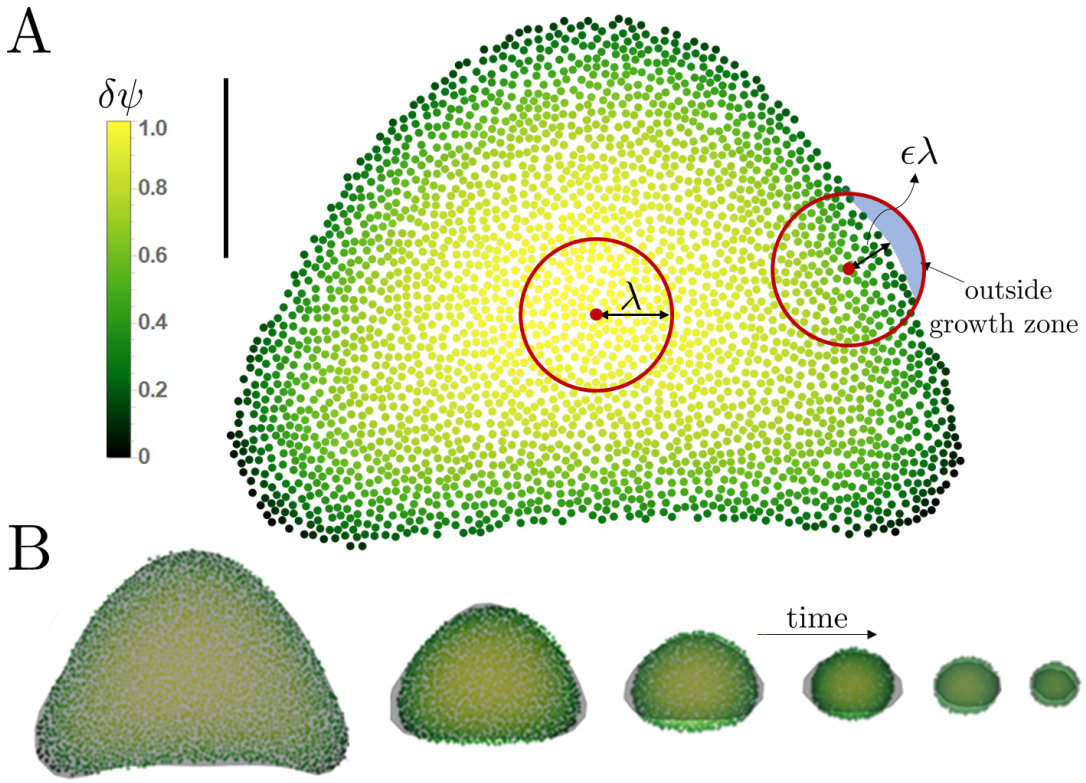

Fig. S12. beak development under the morphogen based boundary and bulk death model. (A) A cross section of a C. *pallidus* beak at $\tau = 0.5$ with a dense packing of 5000 non-overlapping cells, generated by choosing random positions for each cell and removing overlaps. Also shown is the concentration of the morphogen generated by the model described in the text. The range of the morphogen, determined by how far it diffuses before degrading, is controlled by the diffusion coefficient D_c and degradation rate Γ and is given by $\lambda \equiv \sqrt{D_c/\Gamma}$. The perpendicular distance of a cell from the boundary of the growth zone is given by $\epsilon\lambda$. Near the boundary, when $\epsilon \sim 1$, the concentration of the morphogen is less than in the bulk. Scale bar, 1mm. $\delta\psi \equiv (\psi - \psi_{min})/(\psi_{max} - \psi_{min})$ is the concentration, normalized so that it ranges from zero to one in the beak cross section. (B) A comparison of the cross sections generated from this model starting with the cross section in panel (A) as an initial condition. We take the threshold value, which controls when cells near the boundary stop dividing, to be 20% the bulk concentration. The background (bulk) death rate is 5% and $\lambda = 0.1W$. Under these conditions, the size of the growth zone reaches zero in 33 time steps.

In (16) this equation is written without the factor $(t_* - t)^{q-p}$ which is only justified when $q = p$ (see Eq. (9) in Ref. (16)). Fig. S11 shows a direct simulation of a circular growth zone with $\alpha = 2, \beta = 0, \gamma = 1$, $p = 2$ and $q = 1$. The green curves are solutions of Eq. (S.10).

The main fact used to make the prediction $p/q = 1/2$ in (16) is that η and ξ do not change with time (since the time dependent factor $(t_* - t)^{q-p}$ was dropped from the equation). In the time dependent case, the situation is more complicated and analytical solutions are harder to obtain. We can take $p \approx 0.5$ and $q \approx 1$ as inputs from experiment (Fig. S11) and predict what shape we should get from Eq. (S.10). Assuming for simplicity a growth region given by $G = A\eta^2 + \xi^2 + B\eta\,\xi - 1$ (a more general conic would lead to the same result below), we find that the midsagittal section will have the following functional form,

$$z = a\,x + b \pm \sqrt{c\,x + d}\,, \quad a = \tfrac{\beta}{\alpha}\,, \quad b = \tfrac{(B\alpha+2\beta)\gamma^2}{(4A-B^2)\alpha^2}\,,$$
$$c = \tfrac{4(B\alpha+2\beta)\left(A\,\alpha^2+\beta\,(B\,\alpha+\beta)\right)\gamma^2}{\alpha}\,, \quad d = \tfrac{4(B\alpha+2\beta)\left(A\,\alpha^2+\beta\,(B\,\alpha+\beta)\right)\gamma^4}{(4\,A-B^2)\,\alpha^2}. \qquad \text{[S.11]}$$

This functional form fits most of the midsagittal sections of our samples quite well.

Deriving the mean curvature flow from the morphogen based model. Starting with Eq. (6) in the main text, we are led to the following solution

$$\psi(\boldsymbol{\rho}, \tilde{t} \to \infty) \equiv \psi(\boldsymbol{\rho}) = \int_{\mathcal{R}} G(|\boldsymbol{\rho} - \boldsymbol{\rho}'|)\, d^3\boldsymbol{\rho}' = \int_{\mathcal{R}} \frac{e^{-|\boldsymbol{\rho}-\boldsymbol{\rho}'|}}{4\pi|\boldsymbol{\rho}-\boldsymbol{\rho}'|}\, d^3\boldsymbol{\rho}', \qquad \text{[S.12]}$$

where we have allowed for the possibility of a more generic (isotropic) interaction between the cells represented by the function $G(|\boldsymbol{\rho} - \boldsymbol{\rho}'|) > 0$. In deriving the above solution, we assumed that $G(|\boldsymbol{\rho} - \boldsymbol{\rho}'|)$ approaches zero for large separation $|\boldsymbol{\rho} - \boldsymbol{\rho}'| \to \infty$ and the specific form of the solution would be different if we have different boundary conditions, such as $\mathbf{n} \cdot \nabla\psi(\boldsymbol{\rho}) = \mathbf{0}$ when the morphogen is not allowed to pass through the boundary of the growth zone. Note that $\psi(\boldsymbol{\rho}, \tilde{t} \to \infty)$ is maximal in the bulk. In the limit $\lambda \ll W$, we may take the region of integration to be $\mathcal{R} = \mathbb{R}^3$, which gives

$$\psi_{bulk}(\boldsymbol{\rho}, \tilde{t} \to \infty) = \psi_{bulk}(\boldsymbol{\rho}) = \int_{\mathbb{R}^3} G(|\boldsymbol{\rho} - \boldsymbol{\rho}'|)\, d^3\boldsymbol{\rho}' = \int_{\mathbb{R}^3} \frac{e^{-|\boldsymbol{\rho}-\boldsymbol{\rho}'|}}{4\pi|\boldsymbol{\rho}-\boldsymbol{\rho}'|}\, d^3\boldsymbol{\rho}' = 1. \qquad \text{[S.13]}$$

Our goal is to calculate the concentration $\psi(\boldsymbol{\rho})$ a normal distance equal to $\epsilon\lambda$ away from the boundary of the growth zone where the curvature of the cross section is κ (see Fig. S12). We denote this quantity as $\psi_{\epsilon,\kappa}$ and when $\kappa = 0$ it is relatively straightforward to find that

$$\psi_{\epsilon,0} = 2\pi \int_{-\epsilon}^{\infty} dz \int_{0}^{\infty} sds\, G\left(\sqrt{s^2+z^2}\right) = \int_{-\epsilon}^{\infty} dz \int_{0}^{\infty} sds \frac{e^{-\sqrt{s^2+z^2}}}{2\sqrt{s^2+z^2}} = 1 - \frac{e^{-\epsilon}}{2}. \quad [S.14]$$

In performing the integral, we have used polar coordinates with the z-axis perpendicular to the boundary which is located at $z = -\epsilon$ so that the point where we calculate the concentration is at $z = 0$. As before, since $\lambda \ll W$, when calculating the concentration for a point a distance $\epsilon\lambda$ away from the boundary, we may neglect the actual shape of the growth zone and take it to be the half space $z > 0$. Similarly, when $\kappa \neq 0$, we may approximate the growth zone as the region described by $z > \kappa\lambda s^2/2$, where we approximated the segment of the boundary with curvature κ with the parabola $z = \kappa\lambda s^2/2$. In order to obtain the concentration to leading order in κ and ϵ, we make the change of coordinate $z = \zeta + \kappa\lambda s^2/2$. This is convenient since now the boundary sits at $\zeta = 0$. The Jacobian of this transformation is equal to 1 and the integrand of Eq. (S.12) becomes

$$2\pi s\, G\left(\sqrt{s^2 + (\zeta + \kappa\lambda s^2/2)^2}\right) \approx 2\pi s\, G\left(\sqrt{s^2+\zeta^2}\right) + \frac{\pi s^3 \zeta G'\left(\sqrt{s^2+\zeta^2}\right)}{\sqrt{s^2+\zeta^2}}\kappa\lambda + O(\kappa\lambda)^2. \quad [S.15]$$

Since $G(\rho)$ is typically decreasing, $G'(\rho) < 0$, the term proportional to κ is negative as may be intuitively expected. To get the concentration we have to integrate this expression to get

$$\psi_{\epsilon,\kappa} = \int_{-\epsilon}^{\infty} dz \int_{0}^{\infty} ds \left[\frac{se^{-\sqrt{s^2+z^2}}}{2\sqrt{s^2+z^2}} - \frac{s^3 u(1+\sqrt{s^2+z^2})e^{-\sqrt{s^2+z^2}}}{4(s^2+z^2)^{3/2}}\kappa\lambda\right] = 1 - \frac{e^{-\epsilon}}{2} - \frac{e^{-\epsilon}(1+\epsilon)}{2}\kappa\lambda. \quad [S.16]$$

we want to determine the thickness (in units of λ) of the layer of cells that stop dividing (during a cell cycle T_c), which happens when the concentration is below a certain threshold, written as $\psi_{\epsilon,\kappa} \leq f\psi_{bulk}$, where $f < 1$. This thickness is determined by the value of ϵ for which this constraint is satisfied since all cells closer to the boundary than this value will experience lower levels of the morphogen concentration and therefore will also stop division. Solving the equation for ϵ perturbatively, to linear order in κ, we get

$$\epsilon = \log\left(\frac{1}{2(1-f)}\right) + \left[1 + \log\left(\frac{1}{2(1-f)}\right)\right]\kappa\lambda. \quad [S.17]$$

The velocity of the cross section can be written as $\mathbf{v} = -(\epsilon\lambda/T_c)\mathbf{n}$, which gives

$$\mathbf{v} = -(a + b\kappa)\mathbf{n} \implies a = \log\left(\frac{1}{2(1-f)}\right)\frac{\lambda}{T_c}, \quad b = \left[1 + \log\left(\frac{1}{2(1-f)}\right)\right]\frac{\lambda^2}{T_c}. \quad [S.18]$$

Note that both a and b are positive when $f > 1/2$. When f is close to $1/2$, $\epsilon \ll 1$ and we may expand the expression in Eq. (S.16) to leading order in ϵ to get

$$\psi_{\epsilon,\kappa} = \frac{1+\epsilon-\kappa\lambda}{2} = f \implies \epsilon = (2f-1) + \kappa\lambda. \implies a = (2f-1)\frac{\lambda}{T_c}, \quad b = \frac{\lambda^2}{T_c}. \quad [S.19]$$

To show that our conclusion is not sensitive to the choice of the interaction, we also calculate $\psi_{\epsilon,\kappa}$ assuming $G(|\boldsymbol{\rho} - \boldsymbol{\rho}'|) = \Theta(1 - |\boldsymbol{\rho} - \boldsymbol{\rho}'|)$, where $\Theta(1-\rho)$ is a step function that will be zero when $\rho > 1$. In other words, a cell senses all neighbors within a distance λ with equal weight and does not sense cells farther than that. We again assume the range of the morphogen to be much smaller than the size of the beak, $\lambda \ll W$. A cell decides whether it is on the boundary (and whether it should stop dividing) by integrating the effects of its neighbors inside a sphere of radius λ, if a certain fraction of that sphere is not occupied by neighbors (due to being near the boundary), a cell would stop dividing. In this limit, this turns into a geometric problem of computing the overlap volume between two sphere depending on the distance between their centers. One sphere is large with radius κ^{-1} and the other is small with radius λ. This problem can be solved exactly to get the width of the layer of cells that stops dividing at each time instant. The volume occupied by neighbors $\mathcal{V}_N$ as a fraction of the volume $\mathcal{V}_\lambda \equiv 4\pi\,\lambda^3/3$ for a cell that is a distance $\epsilon\,\lambda$ from the boundary is given, to linear order in $\lambda\kappa$ and ϵ, by

[S.20]

This expression gives $1/2$ when $\kappa\lambda = \epsilon = 0$, which corresponds to a sphere cut in half by a plane. Note the fraction $\mathcal{V}_N/\mathcal{V}_\lambda$ is equivalent to $\psi_{\epsilon,\kappa}/\psi_{bulk}$ above. The condition $\mathcal{V}_N < f\,\mathcal{V}_\lambda$ determines whether a cell stops dividing, for some choice of fraction f. Denoting the cell division time as T_c, the velocity can be written as $\mathbf{v} = -(\epsilon\lambda/T_c)\mathbf{n}$ which gives, after solving the condition $\mathcal{V}_N = f\,\mathcal{V}_\lambda$ for ϵ, the modified mean curvature flow with coefficients

$$a = \frac{2(2f-1)}{3}\frac{\lambda}{T_c} > 0, \quad b = \frac{1}{4}\frac{\lambda^2}{T_c} > 0. \quad [S.21]$$

Finally, note that so far in this section we have only considered boundary death, were cell division stops only for cells near the boundary. The effect of bulk death, were cells randomly stop dividing at some rate independent of location, may also be considered. A simulation that combines both boundary and bulk death, is shown in Fig. S12 and Movie S2.

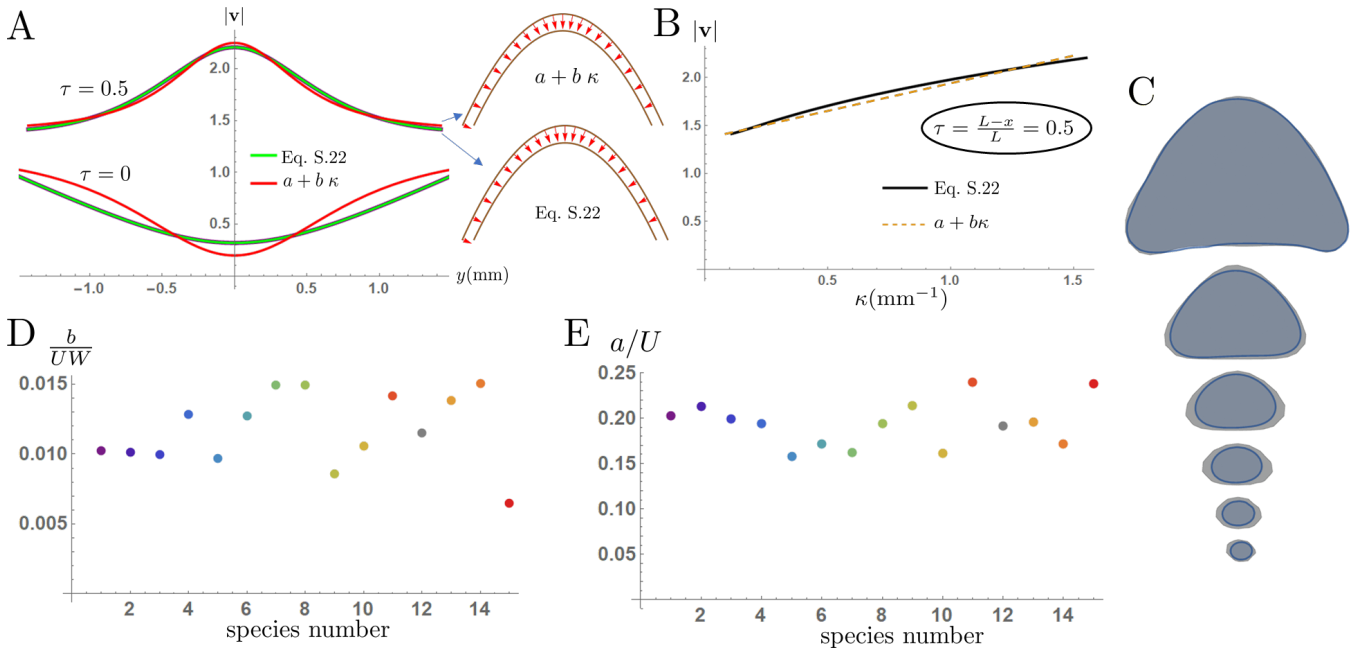

Fig. S13. Modified mean curvature flow approximation for a C. *pallidus* sample. (A) Comparison of the magnitude of the velocity at two different values of τ (time) generated from MMCF (Eq. (S.18) with $a/U = 0.16, b/U = 0.064$mm) and PPF (Eq. (S.22) with parameters $W = 4.3$mm, $D = 2.2$mm, $\tilde{\kappa}_x = 0.86$ and $\tilde{S} = 5.0$). For later times, corresponding to greater τ, the agreement between the two curves improves. Also shown is a comparison of the resulting flows at $\tau = (L - x)/L = 0.5$. Panel (B) shows the approximately linear dependence of speed on curvatures at $\tau = 0.5$, from which the parameters a/U and b/U are extracted (as intercept and slope respectively). (C) Results from a simulation of the MMCF which is being compared to actual cross sections of the beak of C. *pallidus* taken at corresponding values of τ, starting with $\tau = 0.5$. The parameters of the simulation are taken from the linear fit to the plot in panel (B) and correspond to $a/U = 0.16, b/U = 0.064$mm. We get panels (D-E) by repeating the above for all species and extracting the a and b parameters. The species number and color code correspond to the order they appear in Fig. 1 of the main text and Table S1.

Parabola Preserving Flow. In the next two subsections, we look for developmental patterns that can lead to the observed parabolic cross sections.

We start with a cross section of the beak at time $t \geq 0$, which represents the most recently formed part of the beak that has left the growth zone. Since the cross sections are parabolic with changing curvatures and height, we can write the form of the cross section as

$$\mathbf{R}(\Phi, \tau) = \left(x_0(\tau), y(\Phi, \tau), D(\tau) \left[1 - 4\, \frac{y^2(\Phi, \tau)}{W^2(\tau)} \right] \right), \qquad \text{[S.22]}$$

where $D(\tau)$ and $W(\tau)$ are given in the main text (Eqs. 3 & 4). The variable τ is some parameter that parameterizes the different transverse cross sections along the length of the beak. It could be taken as the real developmental time t or the distance along the proximal-distal axis of the most recently formed section $x_0(t)$, as illustrated in Fig. 3B. The function $x_0(t)$, which is the center of mass of the growth zone at time t ($\dot{x}_0(t) \equiv -U(t)$), relates the position of the cross section to real developmental time. In the following, the variable τ will be taken as the dimensionless quantity $\tau \equiv \frac{L - x_0(t)}{L}$. Similarly, Φ parameterizes the transverse cross section at a fixed value of τ. A biologically motivated choice of the parameter Φ is the angle illustrated in Fig. 4D of the main text. The distance of a point on the boundary from the center of the growth zone can be written as

$$R(\Phi) = \frac{|\sec(\Phi)|}{\sqrt{32}} \frac{W(\tau)}{D(\tau)} \sqrt{8D(\tau)^2 + \tan^2(\Phi) W^2(\tau) - W(\tau) |\tan(\Phi)| \sqrt{16D(\tau)^2 + W^2(\tau) \tan^2(\Phi)}}. \qquad \text{[S.23]}$$

We seek an expression for the velocity field $\boldsymbol{v}(\Phi, \tau) \equiv \partial_\tau \mathbf{R}(\Phi, \tau)$, which describes the cell division polarity, or the direction of motion of the cells which will form the next cross section along the beak. It is natural to assume that the velocity, $\boldsymbol{v}(\Phi, \tau) \equiv \partial_\tau \mathbf{R}(\Phi, \tau)$, is normal to the cross section. This would be the only choice if the growth law is geometric, that is, the change in shape depends on the current shape through its first and second derivatives. In any case, it is always possible to change coordinates ($\Phi \to \Phi'$) so that the velocity tangent to the curve is zero.

Since we know the shape of the upper part of the beak Eq. (S.22), we can use that to get insight into the actual developmental growth law involved. We refer to the flow in Eq. (S.22) as the parabola preserving flow (PPF) since it consists of parabolas at every point in time[†]. Fig. S13 shows the velocity field $\boldsymbol{v}(\Phi, \tau)$ extracted directly from the morphometric form Eq. (S.22). When plotted against the curvature of the upper part of the beak, it is approximately linear across the range of curvatures

[†] It can be shown that such a flow is generated from a velocity field $\boldsymbol{v}(\Phi, \tau)$ that depends on $\kappa^{\pm 1/3}$.

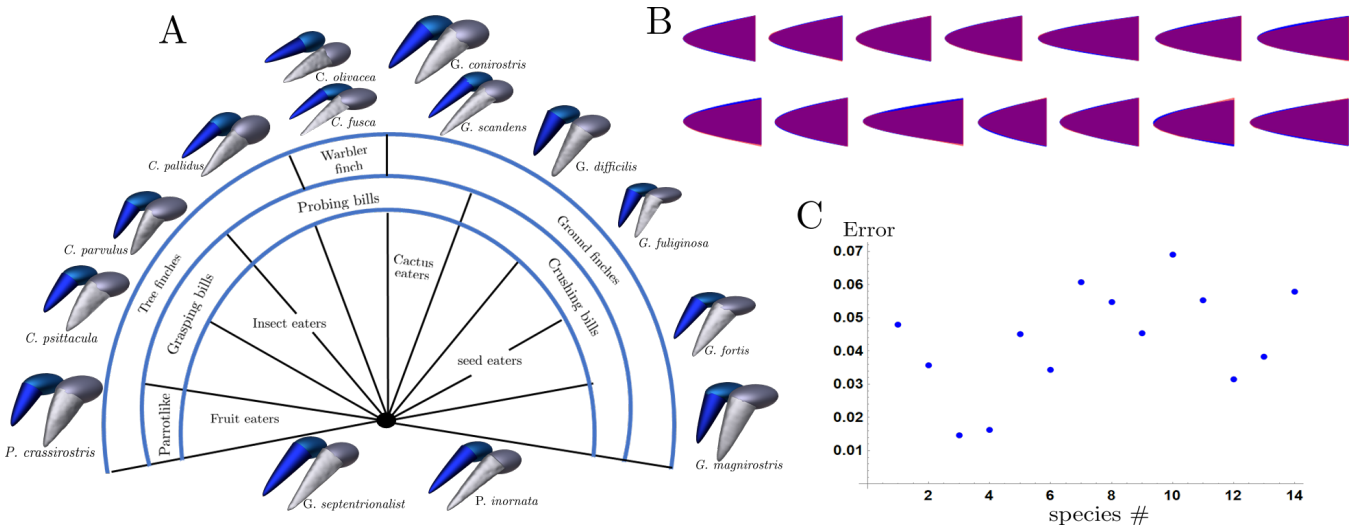

Fig. S14. Comparison of beaks generated using MMCF applied to circular cross sections. (A) An illustration of the relation between morphology and feeding behavior. Note that probing beaks tend to be sharper at the tip (smaller value of the parameter b) and a higher length to width ratio. Furthermore, these beaks also tend to be more aligned with the axes of the skull. On the other hand, beaks that rely on biting force such as P. *crassirostris* and G. *magnirostris* have beaks that are oriented significantly away from the skull (60 degrees in the case of G. *magnirostris*) and will be broader and more curved near the tip. Panels (B) & (C) compare the generated beaks (blue), corresponding to Eq. (S.25) with parameters given in Table S2, with the scanned beaks (projected onto the xy-plane, purple). See also Fig. 5 in the main text. The error plotted in (C) is the area of the non-overlapping region in (B) relative to the total area from the actual beaks (purple).

involved, suggesting as we show next that the mean curvature flow can be used to model the beak development. Table S1 records the fitting results for all samples.

Modified Mean Curvature Flow Approximates Beak Development. We wish to discover to what extent $\mathbf{v}\cdot\hat{n} = -(a + b\,\kappa)$, can describe the behavior of the beak cross sections over time (both a and b are positive). The mean curvature (also referred to as curve-shortening) flow is a variant of this evolution equation with $a = 0$. Therefore, we refer to the growth law as modified mean curvature flow (MMCF). It is convenient to work with the MMCF compared with PPF since it has simple dependence on curvature and is well studied mathematically, at least for the case $a = 0$. Furthermore, such a flow results from a gradient decent generated by the energy

$$\mathcal{E}[\mathbf{R}] = a\,\mathcal{A}[\mathbf{R}] + b\,\mathcal{L}[\mathbf{R}], \qquad [S.24]$$

where $\mathcal{A}[\mathbf{R}]$ is the area enclosed by the curve $\mathbf{R}(\Phi,\tau)$ and $\mathcal{L}[\mathbf{R}]$ is its length. Thus, it will be easier to connect the parameters of this law, which also emerges generically in reaction diffusion systems (17–20), to cellular level processes involving morphogen diffusion.

In order to determine whether the MMCF can explain the evolution of the beak cross sections, we first compare it to the PPF flow Eq. (S.22), which does explain the growth of the top (parabolic) part of the cross sections. For the majority of the beak, apart from a region near the base, the two flows generate approximately the same velocity field (Fig. S13). Therefore, we linearly fit the function $\mathbf{v}(\kappa)$ to obtain the parameters a and b to be used in the simulation below. Note that there is another, inequivalent way to determine a and b from a slightly different model that uses the behavior of circular cross sections near the tip as explained below.

Motivated by the linear fit of $\mathbf{v}(\kappa)$, we numerically simulated the MMCF evolution with the cross section of a C. *pallidus* sample at $\tau = 0.5$ as an initial configuration. The level-set method described in (21) was used to simulate the flow. As seen in Fig. S13, with constant values of a and b this flow does a good job of capturing the behavior of the cross sections. Note in particular that the initially non-convex cross section evolves into a convex section and proceeds to become rounder over time while shrinking in size. This behavior is expected generically for the mean curvature flow of curves (22). We can repeat the above to obtain the parameters shown in Fig. S13 and Table S1. Note that the dimensionless growth parameters shown are nearly constant for the ground finches, despite very different sizes, possibly indicating a common developmental mechanism. The value $b/(UW) \sim 0.01$ is very close to that estimated from the cellular model of growth in the main text (Material and Methods).

Another useful simplification of our growth model involves assuming semi-circular cross sections. While circular shapes do not fit the transverse cross sections of the beak as well as parabolas (Fig. S3), this will yield useful insights since it can be solved analytically. The MMCF equations become

$$\dot{R}(t) = -a - \frac{b}{R(t)}, \quad \tau \equiv \frac{L - x_0(t)}{L} = \frac{Ut}{L}, \quad R(\tau) = \frac{W(\tau)}{2}. \qquad [S.25]$$

When deriving the relation between τ and time we assume $\dot{x}_0(t) = -U$ is a constant in time, as justified experimentally (Fig. S11). We perform the change of variables to the parameter τ to compare with Eq. (4) in the main text and use that to

Number	Species	$b/(UW)$	a/U
1	G. *fuliginosa*	0.01	0.2
2	G. *fortis*	0.01	0.21
3	G. *magnirostris*	0.01	0.2
4	G. *conirostris*	0.013	0.19
5	G. *scandens*	0.01	0.16
6	G. *septentrionalist*	0.013	0.17
7	C. *pallidus*	0.015	0.16
8	C. *parvulus*	0.015	0.19
9	C. *psittacula*	0.009	0.21
10	P. *inornata*	0.011	0.16
11	P. *crassirostris*	0.014	0.24
12	G. *difficilis*	0.012	0.19
13	C. *olivacea*	0.014	0.2
14	C. *fusca*	0.015	0.17
15	T. *bicolor*	0.007	0.24

Table S1. The quantities $b/(UW)$ and a/U extracted directly from the linear fit of the relation between the speed v and curvature κ, as shown in Fig. S13.

Species	W (mm)	L/W	$b/(UW)$	Angle (degrees)	$b/(aW)$
G. *fuliginosa*	3.6	1.7	0.047	56	0.48
G. *fortis*	4.9	1.6	0.043	44	0.43
G. *magnirostris*	6.5	1.7	0.046	59	0.49
G. *conirostris*	5.1	1.7	0.052	36	0.86
G. *scandens*	4.6	2.3	0.037	31	0.64
G. *septentrionalist*	4.1	1.9	0.041	35	0.55
C. *pallidus*	3.8	2.08	0.049	27	1.51
C. *parvulus*	3.27	1.67	0.061	48	1.47
C. *psittacula*	4	1.5	0.068	38	1.48
P. *inornata*	3.2	2.2	0.039	32	0.70
P. *crassirostris*	5.5	1.4	0.064	47	0.89
G. *difficilis*	3.8	1.6	0.050	48	0.60
C. *olivacea*	2.7	1.6	0.056	9	1.55
C. *fusca*	2.45	2.1	0.037	24	0.55

Table S2. The quantities L/W and $b/(UW)$ plotted in Fig. S14 and the angle relative to the skull calculated for a representative member from each species.

extract the parameters a and b. Note that we chose to compare $R(\tau)$ to $W(\tau)$ (instead of $D(\tau)$) since near the tip they both will have the same analytical form (Eq. (10) in the main text) which allowed us to explicitly relate the parameters a and b to morphometric parameters. Fig. S14 shows a comparison of beaks generated using MMCF applied to circular cross sections. The parameter b extracted here is larger (and a correspondingly smaller) compared with the results of Fig. S13. Extracting the parameter b this way gives us a developmental constraint satisfied by all the samples. The quantities L/W and b/W plotted in Fig. S14 and the angles relative to the skull calculated for a representative member from each species are provided in Table S2.

Dataset

SI Dataset S1 (Datasets/dataset_one.txt)

Morphospace generated by the parameters $(L, W, D, \tilde{\kappa}_x, \tilde{S})$. Each row in the dataset corresponds to one of the 59 samples. Raw mesh data and all code used to generate these results are available at https://doi.org/10.7910/DVN/IHODX1.

References

1. A Pumarola, J Sanchez-Riera, GPT Choi, A Sanfeliu, F Moreno-Noguer, 3DPeople: Modeling the geometry of dressed humans in *Proc. IEEE Int. Conf. Comput. Vis.* pp. 2242–2251 (2019).
2. DJ Kroon, Polygon2Voxel (https://www.mathworks.com/matlabcentral/fileexchange/24086-polygon2voxel) (2009).
3. A Sinha, J Bai, K Ramani, Deep learning 3D shape surfaces using geometry images in *Comput. Vis. ECCV*. (Springer), pp. 223–240 (2016).
4. A Jacobson, gptoolbox - Geometry processing toolbox (https://github.com/alecjacobson/gptoolbox) (2015).
5. U Pinkall, K Polthier, Computing discrete minimal surfaces and their conjugates. *Exp. Math.* **2**, 15–36 (1993).

6. Q Fang, Iso2Mesh: a 3D surface and volumetric mesh generator for MATLAB/Octave (http://iso2mesh.sourceforge.net) (2008).
7. P Virtanen, et al., SciPy 1.0: Fundamental algorithms for scientific computing in Python. *Nat. Methods* **17**, 261–272 (2020).
8. MP Dubuisson, AK Jain, A modified Hausdorff distance for object matching. *Proc. 12th Int. Conf. on Pattern Recognit.* **1**, 566–568 (1994).
9. O Campàs, R Mallarino, A Herrel, A Abzhanov, MP Brenner, Scaling and shear transformations capture beak shape variation in Darwin's finches. *Proc. Natl. Acad. Sci.* **107**, 3356–3360 (2010).
10. PR Grant, The feeding of Darwin's finches on Tribulus cistoides (L.) seeds. *Anim. Behav.* **29**, 785–793 (1981).
11. A Pogorelov, *Bendings of Surfaces and Stability of Shells*, MMONO Series. (American Mathematical Society), (1988).
12. H Hertz, Ueber die berührung fester elastischer körper (On contact between elastic bodies). *J. für die reine und angewandte Math.* **1882**, 156–171 (1882).
13. B Audoly, Y Pomeau, Elasticity and geometry: from hair curls to the nonlinear response of shells (2010).
14. Y Seki, MS Schneider, MA Meyers, Structure and mechanical behavior of a toucan beak. *Acta Mater.* **53**, 5281–5296 (2005).
15. J Soons, et al., Multi-layered bird beaks: a finite-element approach towards the role of keratin in stress dissipation. *J. R. Soc. Interface* **9**, 1787–1796 (2012).
16. JA Fritz, et al., Shared developmental programme strongly constrains beak shape diversity in songbirds. *Nat. Commun.* **5**, 1–9 (2014).
17. JP Keener, A geometrical theory for spiral waves in excitable media. *SIAM J. Appl. Math.* **46**, 1039–1056 (1986).
18. JJ Tyson, JP Keener, Singular perturbation theory of traveling waves in excitable media (a review). *Phys. D* **32**, 327–361 (1988).
19. J Rubinstein, P Sternberg, JB Keller, Fast reaction, slow diffusion, and curve shortening. *SIAM J. Appl. Math.* **49**, 116–133 (1989).
20. P Grindrod, MA Lewis, JD Murray, A geometrical approach to wave-type solutions of excitable reaction-diffusion systems. *Proc. R. Soc. A* **433**, 151–164 (1991).
21. R Kimmel, G Sapiro, Shortening three-dimensional curves via two-dimensional flows. *Comput. Math. Appl.* **29**, 49–62 (1995).
22. MA Grayson, The heat equation shrinks embedded plane curves to round points. *J. Diff. Geom.* **26**, 285–314 (1987).